Low energy measurement of the ^{14}N(p, γ)^{15}O total cross section at the LUNA underground facility

LUNA Collaboration

D. Bemmerer [a], F. Confortola [b], A. Lemut [b], R. Bonetti [c], C. Broggini [a],
P. Corvisiero [b], H. Costantini [b], J. Cruz [d], A. Formicola [e], Zs. Fülöp [f],
G. Gervino [g], A. Guglielmetti [c], C. Gustavino [e], Gy. Gyürky [f],
G. Imbriani [h], A. Jesus [d], M. Junker [e], B. Limata [h], R. Menegazzo [a],
P. Prati [b,*,1], V. Roca [h], C. Rolfs [i], D. Rogalla [h], M. Romano [h],
C. Rossi-Alvarez [a], F. Schümann [i], E. Somorjai [f], O. Straniero [j],
F. Strieder [i], F. Terrasi [k], H.P. Trautvetter [i]

[a] *INFN Sezione di Padova, Padova, Italy*
[b] *Università degli Studi Genova & INFN Genova, Genova, Italy*
[c] *Università di Milano & INFN Milano, Istituto di Fisica Generale Applicata, Milano, Italy*
[d] *Centro de Fisica Nuclear da Universidade de Lisboa, Lisboa, Portugal*
[e] *INFN, Laboratori Nazionali del Gran Sasso, Assergi, L'Aquila, Italy*
[f] *ATOMKI, Debrecen, Hungary*
[g] *Università di Torino & INFN Torino, Torino, Italy*
[h] *Università "Federico II" & INFN Napoli, Napoli, Italy*
[i] *Institut für Experimentalphysik III, Ruhr-Universität Bochum, Bochum, Germany*
[j] *INAF, Osservatorio Astronomico di Collurania, Teramo, and INFN Napoli, Napoli, Italy*
[k] *Seconda Università di Napoli & INFN Napoli, Napoli, Italy*

Abstract

Deep underground in Gran Sasso National Laboratory (Italy), at the LUNA facility, the cross section of the ^{14}N(p, γ)^{15}O, the slowest process of the CNO cycle, has been measured at energies much lower than

* Corresponding author. Tel.: +39 010 353 6439; fax: +39 010 314218.
 E-mail address: prati@ge.infn.it (P. Prati).
1 Present address: Dipartimento di Fisica, Via Dodecaneso 33, 16146 Genova, Italy.

achieved before. Using a 400 kV accelerator, a windowless gas target and a 4π BGO summing detector, direct cross section data has been obtained down to 70 keV, reaching a value of 0.24 picobarn, corresponding to an S-factor of 1.74 ± 0.14(stat) ± 0.14(syst) keV barn. The Gamow peak has been covered by direct experimental data for several scenarios of stable and explosive hydrogen burning. The $\omega\gamma$ strength of the 259 keV resonance has been re-measured obtaining 12.8 ± 0.3(stat) ± 0.4(syst) meV. The stellar reaction rate has been calculated for temperatures $0.09 \times 10^9 - 0.3 \times 10^9$ K. A complete description of the experiment is here presented, including the impact of the present data on nucleosynthesis in AGB stars.

1. Introduction

Stars generate energy and synthesize chemical elements in thermonuclear reactions [1]. Non-resonant reactions induced by charged particles in a star take place in a narrow energy window called the Gamow peak, far below the Coulomb barrier.

At low energy, the cross section $\sigma(E)$ of a charged particle induced reaction drops steeply with decreasing energy due to the Coulomb barrier in the entrance channel [1]:

$$\sigma(E) = S(E)\frac{e^{-2\pi\eta(E)}}{E}, \tag{1}$$

where $S(E)$ is the astrophysical S factor, and η is the Sommerfeld parameter with $2\pi\eta = 31.29\, Z_1 Z_2(\mu/E)^{1/2}$. Here Z_1 and Z_2 are the charge numbers of projectile and target nucleus, respectively, μ is the reduced mass (in amu units), and E is the center of mass energy[2] (in keV units).

Generally, $\sigma(E)$ has a very low value at the Gamow peak, this preventing a direct measurement in a laboratory at the Earth's surface, where the signal to background ratio is too small because of cosmic ray interactions with detectors. Hence, cross sections are usually measured at high energies and expressed as the astrophysical S factor from Eq. (1). The S factor is then used to extrapolate the data to the Gamow peak region. Although $S(E)$ varies only slowly with energy for the direct process, resonances and resonance tails may hinder the extrapolation, resulting in large uncertainties [1]. Therefore, the primary goal of experimental nuclear astrophysics remains to measure the cross section at energies inside the Gamow peak, or at least to approach it as closely as possible.

The Laboratory for Underground Nuclear Astrophysics (LUNA) has been designed for this purpose and is located deep underground in the Laboratori Nazionali del Gran Sasso (LNGS)[3] in Italy. The Gran Sasso site is protected from cosmic rays by a rock cover (1400 m thick) equivalent to 3800 m water, suppressing the flux of cosmic ray induced muons by six orders of magnitude [2] and the neutron flux by three orders of magnitude [3]. Using this approach, in combination with high current accelerators [4,5] and high efficiency detection systems, two hydrogen burning reactions were studied for the first time directly in their respective solar Gamow peak: the ^{3}He(^{3}He, 2p)^{4}He [6] and the ^{2}H(p, γ)^{3}He reaction [7].

---

[2] In the present work, E denotes the energy in the center of mass system, and E_{beam} is the projectile energy in the laboratory system.
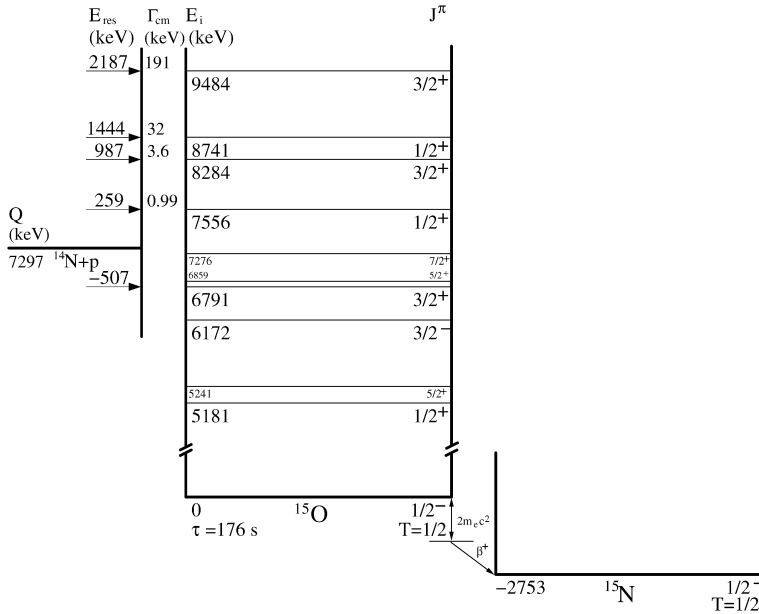
[3] http://www.lngs.infn.it.

Fig. 1. Relevant level scheme of ^{15}O near the ^{14}N$(p, \gamma)^{15}$O threshold [9].

In the present work, an experimental study of the radiative capture reaction ^{14}N$(p, \gamma)^{15}$O ($Q = 7297$ keV [8]) at low energy is presented. The relevant nuclear levels of ^{15}O are shown in Fig. 1. In a low metallicity star, in the temperature range of $0.02 - 0.13 T_9$ (T_9 is the temperature in units of 10^9 K), the stellar hydrogen burning is dominated by the CNO cycle, and its rate is determined by the rate of the slowest process, the ^{14}N$(p, \gamma)^{15}$O reaction. This temperature range corresponds to Gamow peak energies of 30–110 keV (maximum of the Gamow peak location) for the ^{14}N$(p, \gamma)^{15}$O.

There have been many experimental studies of the ^{14}N$(p, \gamma)^{15}$O reaction at low energies [10–15]. Only one of the previous studies obtained data that was at the edge of the astrophysically relevant energy region, with 50% statistical uncertainty for the cross section values [11]. The other studies obtained data only at energies above the astrophysical range and generally the results are then extrapolated in the framework of the R-matrix model down to stellar energies. The standard cross section value used in recent reaction rate compilations [16–18] is mainly based on the data of Schröder et al. [15], with data down to $E = 181$ keV, and on the low energy total cross sections from Ref. [11].

Recently, the results of Schröder et al. [15] for capture to the ground state in ^{15}O have been revised downward by several works, on theoretical [19] and indirect grounds [20–23].

In our first study of ^{14}N$(p, \gamma)^{15}$O, titanium nitride solid targets and a high purity germanium detector were used to measure the cross sections for capture to the five most important states in ^{15}O (see Fig. 1), including the ground state, down to $E = 119$ keV [9,24] although with limited precision. This energy is much lower than has been reached in any previous study for the ground state transition. The revised extrapolation indicates an S factor at astrophysical energies that is half of the values adopted in reaction rate compilations [16–18], leading to considerable astrophysical consequences [25–27]. A recent and independent experiment confirmed this revision with the lowest energy point for the ground state transition at $E = 187$ keV [28].
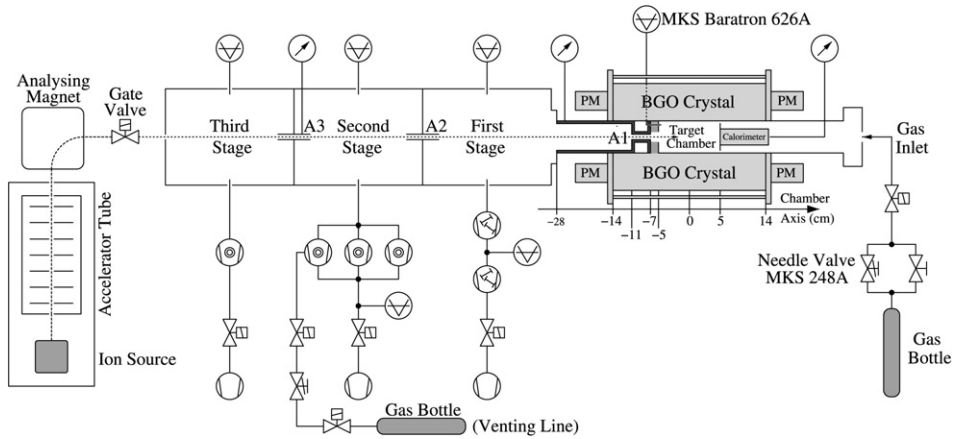
Fig. 2. Schematic drawing of the setup with windowless gas target and BGO detector [32].

Here we describe the second phase of the ^{14}N(p, γ)^{15}O study, using a windowless gas target setup and a 4π BGO summing crystal. We report on a measurement of the ^{14}N(p, γ)^{15}O total cross section at energies as low as $E = 70$ keV and on a new measurement of the $\omega\gamma$ strength of the resonance at $E_R = 259$ keV. We give upper limits on strength of narrow resonances for $E_{beam} = 80$–150 keV, as well as the astrophysical reaction rates based directly on present experimental data. We discuss astrophysical scenarios where the present data have a direct impact.

We present here all the details of the experiment and final data analisys previously published in abbreviated form [29]. Additional details of the experiment can be found in Refs. [30,31].

2. The experimental setup

2.1. Accelerator and windowless gas target

The LUNAII 400 kV accelerator has been described elsewhere [5]. The machine is able to provide up to 500 µA of proton beam in the target chamber over a continuous operating time of about 40 days. The accelerator beam energy uncertainty has been found to be 0.1 keV statistical and 0.3 keV systematic [5]. The long term stability is 5 eV/h [5].

In this experiment the accelerator delivered a proton beam to a differentially pumped windowless gas target (Fig. 2), the γ-rays were detected by a 4π BGO summing crystal. A similar vacuum system and the BGO detector have been described previously [32]; in the following we summarize the main characteristics of the setup.

The beam enters the target chamber through three pumping stages separated by apertures of increasing flow impedance (A3, A2, and A1 in Fig. 2). The collimator at the target entrance (A1) is 40 mm long with a diameter of 7 mm. The pressure drop between the target cell and the first pumping stage must be as high as possible (here it is larger than a factor 70) since capture reactions occuring in this segment of the beam line produce photons that can be detected by the BGO detector with relatively high efficiency (Fig. 2). This undesired γ-ray flux is proportional, at a given beam energy, to the product of the beam current in the first pumping stage and the gas pressure profile in that segment of the beam line (see Section 3.2). The target chamber has one port for gas inlet and one extended port for pressure measurement (target reference pressure): A Cu pipe of 30 cm length and 6 mm inner diameter connects the target chamber to a MKS

Baratron capacitance manometer with an accuracy of 0.25%, located outside the BGO detector (Fig. 2). The nitrogen pressure in the target chamber is kept constant within 0.5% by a needle valve (Fig. 2) in combination with an active electronic feedback regulation system.

The BGO detector is shaped as a 28 cm long cylinder with a coaxial hole of 6 cm diameter. The crystal is divided into 6 optically indepedent sectors (radial thickness 7 cm), each covering an azimuthal angle of 60 degrees. Two Hamamatsu R1847-07 photomultipliers (PMs) are coupled to the opposite faces of each sector. The target chamber and the beam calorimeter are hosted inside the BGO hole (Fig. 2). The center of the 10 cm long target cell is at the middle of the detector. This way the detector covers a large fraction of the solid angle (97.7%).

2.2. Beam current integration

The beam current in the target area was determined using a beam calorimeter with constant temperature gradient [32]. The use of a Faraday cup is here prevented since in passing through the different pumping stages of the gas target system the charge state of low energy projectiles fluctuates [33]. The power delivered by the beam (and consequently the number of projectiles) is calculated as the difference between heating power without beam (W_{no_beam}) and with ion beam (W_{beam}). Thus, the number of accelerated proton in a run is given by:

$$N_p = \frac{(W_{no\_beam} - W_{beam})}{E_{cal}} \times \Delta t, \tag{2}$$

where E_{cal} is the laboratory energy of the beam projectiles at the calorimeter surface, and Δt the measurement time. E_{cal} is calculated according to the stopping power tabulation of Ref. [34] and to the effective target density discussed in the next section. The calorimeter has been designed to measure beam powers in the range 10–140 W. It has been calibrated at the LUNAII 400 kV accelerator with a systematic uncertainty smaller than 1% [32].

2.3. Effective target density

The gas pressure P and temperature T vary along the beam path from the accelerator to the interaction chamber and the target density (in units of atoms/cm^3) at position z is given by [1]:

$$\rho(z) = \frac{\nu P(z)}{kT(z)}, \tag{3}$$

where ν is the number of atoms per molecule and k is the Boltzmann constant. The pressure profile in the first pumping stage and in the target chamber was measured with a dedicated setup (shown in Fig. 2 of Ref. [32]) using a couple of manometers with an accuracy of 0.25%. The pressure drop along the Cu pipe connecting the manometer to the target chamber was found smaller than 0.5%. In the pipe sections where direct pressure measurements were impossible (i.e. inside the 40 mm long collimator at target entrance) linear pressure gradients were assumed.

The gas temperature profile without beam was measured in the target chamber with a special low thermal capacity PT100 temperature transducer, shielded against thermal radiative effects, with an accuracy of 0.1 C°. The resulting density profile without beam, $\rho(z)$, is shown in Fig. 5; $\rho(z)$ values are affected by statistical and systematic uncertainties of 0.25% and 0.5%, respectively.

When the beam passes through the nitrogen gas the local density can be reduced due to temperature and other effects at intense ion beam [35]. Moreover, pressure and temperature
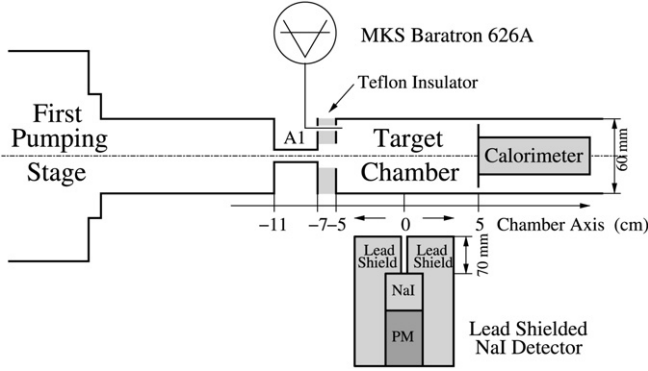
Fig. 3. Setup used to study the beam heating effect. See text for details.

gauges cannot be used in conjunction with the beam to detect changes in the local area along the beam path. We measured the local gas density with and indirect method [35] exploiting the $E_R = 259$ keV resonance in the ^{14}N(p, γ)^{15}O reaction.

The local density is related to the energy loss ΔE_{beam} by:

$$\Delta E_{\text{beam}} = E_{\text{beam}}(z_R) - E_R = \int_0^{z_R} \frac{dE}{d(\rho x)}\big(E(z)\big)\rho_{\text{beam}}(z)\,dz, \tag{4}$$

where $E_{\text{beam}}(z_R)$ is the proton energy at the accelerator resulting, due to the energy loss in the gas target, in $E = 259$ keV at position z_R along the beam path, E_R is the resonance energy, $\frac{dE}{d(\rho x)}$ is the proton stopping power in nitrogen [34], and ρ_{beam} is the actual target density with the beam.

To take into account the beam heating effect in the nitrogen gas we introduced a correction factor h_{beam} defined by:

$$\rho_{\text{beam}}(z) = h_{\text{beam}}(z) \times \rho(z), \tag{5}$$

where $\rho(z)$ is the gas density profile measured without beam. Combining Eqs. (4) and (5), and assuming h_{beam} as constant with position (see later), the correction factor is given by:

$$h_{\text{beam}} = \frac{\Delta E_{\text{beam}}}{\Delta E}, \tag{6}$$

where ΔE_{beam} is the proton energy loss given by Eq. (4), and ΔE is the energy loss calculated with the density profile measured without beam.

To measure ΔE_{beam} we used a lead shielded $1'' \times 1''$ NaI detector mounted on a slit movable along an axis parallel to the beam direction (Fig. 3). The lead shield had an hole of 5 mm diameter and was 70 mm thick. The effective target length seen by the collimated detector was determined, with the LUNA Monte Carlo code [36], to be 2.00 ± 0.14 cm (FWHM of the spatial efficiency distribution for 7 MeV γ-rays).

To determine at which beam energy the resonance is located at z_R in front of the NaI detector, the resonance scan technique was used: The proton beam energy E_{beam} was changed in fine steps (500 eV) for getting the excitation functions and consequently the maximum of the yield.

The scans were repeated at several detector position along the target chamber, namely -5, -3, -1, 1, and 3 cm (see Figs. 2 and 3). At each position the measurements were performed at
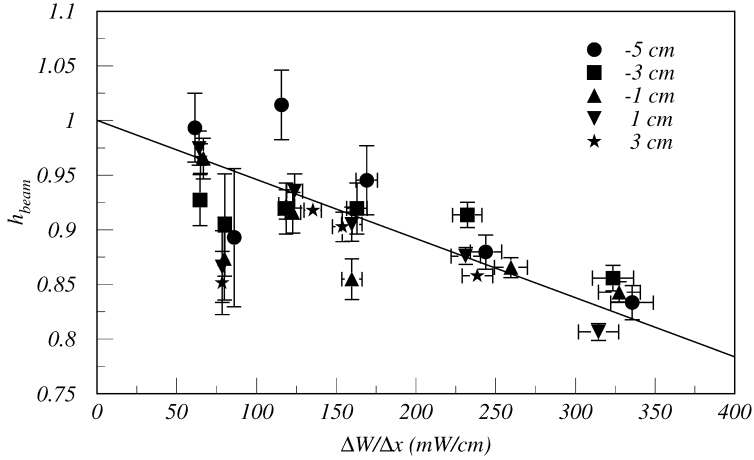
Fig. 4. Beam heating correction factor h_{beam} as a function of the dissipated power per unit length in the nitrogen gas [35] for different positions along the beam path (Fig. 2). Error bars do not include the systematic uncertainty of the beam energy loss ΔE_{beam}. The solid line through the data points assumes a linear relationship between the correction factor and dW/dx.

several pressures, (0.5, 1.0, and 2.0 mbar) and with different beam intensities. For each resonance scan, we calculated the density correction factor h_{beam} (Eq. (6)). The results are plotted in Fig. 4 as a function of the dissipated power per unit length dW/dx [35]:

$$\frac{dW}{dx} = \frac{dE}{dx} \times I_p, \tag{7}$$

where $\frac{dE}{dx}$ is the proton energy loss per unit length [34], and I_p is the proton beam intensity.

The h_{beam} values are mainly affected by the systematic uncertainties due to the determination of the energy loss ΔE_{beam} (see Eq. (4)) that ranged from 35% at 0.5 mbar, through 16% at 1 mbar to 7% at 2.0 mbar (not shown in Fig. 4).

No sizeable h_{beam} dependence on the position has been observed (Fig. 4). This is in agreement with the conclusions in Ref. [35]. In fact, a 10% variation in the target density $\rho(z)$ (Fig. 5) would result in a change of h_{beam} smaller than 2%, well below other experimental uncertainties.

As in Ref. [35] we assumed a linear relationship between h_{beam} and dW/dx (Fig. 4) obtaining:

$$h_{\text{beam}} = 1.0 - 5.4 \times 10^{-4} \left(\frac{dW}{dx} \right), \tag{8}$$

where dW/dx is in units of mW/cm. The total uncertainty of the h_{beam} factor given by Eq. (8) is 3.2%, given by the average deviation between the adopted linear interpolation and the experimental values.

The effective target density profile, including the beam heating effect, is shown in Fig. 5.

2.4. BGO detector and LUNA Monte Carlo simulation

In the experiment the signals from the six BGO sectors were summed to give the spectrum of the total γ-rays energy emitted per event. The performance of the BGO detector were simulated with the LUNA Monte Carlo code [36] and its predictions were tested in terms of detection efficiency $\eta(z)$ and spectrum shape. The code had also been extensively tested in the past [6,7,
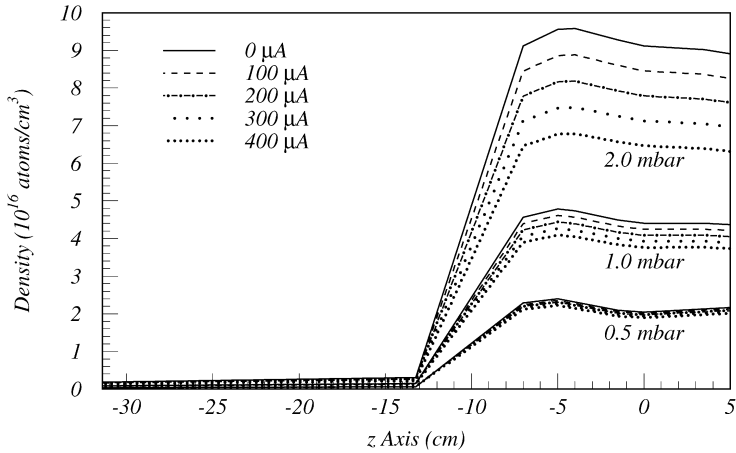
Fig. 5. Effective target density profile along the beam path for three typical nitrogen pressures (0.5, 1.0, and 2.0 mbar). Profiles obtained with different beam current values are shown. The *z* axis is the same as on Figs. 2 and 3.
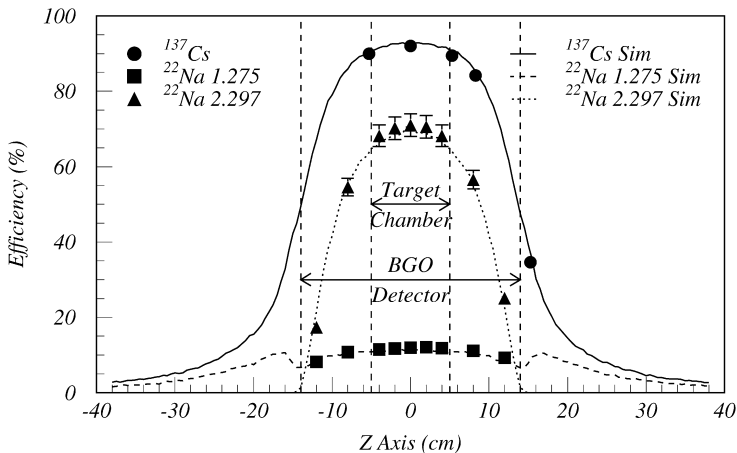

Fig. 6. BGO efficiency; full circles: experimental efficiency measured with a calibrated ^{137}Cs radioactive source (activity uncertainty 1.5%) in several positions along the beam axis; full squares: [22]Na 1.275 MeV line (source activity uncertainty 3.7%); full triangles: [22]Na 2.297 MeV summing peak; solid, dashed and dash-dot lines are LUNA Monte Carlo predictions for ^{137}Cs, [22]Na 1.275 MeV and [22]Na 2.297 MeV peaks, respectively (uncertainty 1.5%). The vertical lines represent the extension of the target chamber and BGO crystals (Fig. 2).

37]; in this experiment we compared the detection efficiency with experimental values of $\eta(z)$ (Fig. 6) obtained moving point-like calibrated radioactive sources (^{137}Cs and [22]Na) along the beam path inside the bore-hole of the BGO detector (Fig. 2). The ^{137}Cs source has been chosen because it emits mono-energetic γ-rays and for the high accuracy of its calibration (1.5%) while the [22]Na (calibration accuracy 3.7%) has been used to check the code capability in describing the summing properties of γ-rays cascades (see later). We quote a 1% systematic uncertainty due to the approximations in the description of the setup geometry and materials.

The BGO detector covers a large solid angle and thus primary and secondary γ's arising from transitions to intermediate states of [15]O get summed with high probability in a peak at
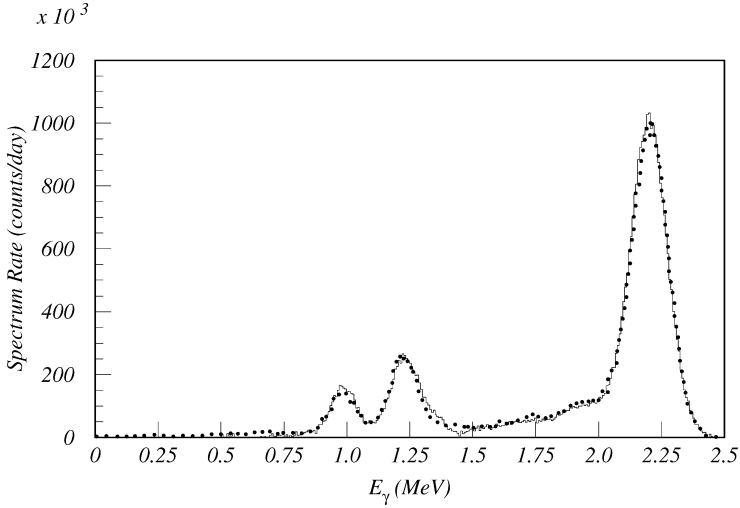
Fig. 7. ^{22}Na spectrum (solid line, normalized to running time) compared with a simulation (dotted line, normalized to the height of the 2.297 MeV experimental summing peak). The peak at 1.022 MeV is the sum of the two annihilation γ's, the peak at 1.275 MeV is the dexcitation of the 1.275 MeV level of ^{22}Ne, and the peak at 2.297 MeV is the sum of the two annihilation γ's with the 1.275 MeV line (summing peak). The source was at the center of the target chamber.

$E_\gamma = Q + E_{cm}$; $Q = 7.297$ MeV for ^{14}N$(p, \gamma)^{15}$O. Spectrum shape and detection efficiency depend on the decay probability to intermediate states of ^{15}O (see Section 3.2). Similarly it happens in case of a radioactive source, where the detector summing properties depends on well-known branching ratios.

The Monte Carlo code generates, event by event, γ-cascades depending on given branching ratio (for the ^{14}N$(p, \gamma)^{15}$O varying with beam energy). Details of the angular distribution and of the branching ratio adopted are discussed in Section 3.2, where all the source of uncertainties are presented (see Table 1). The γ-cascades are tracked through passive materials and into the BGO crystals until they are absorbed by the detector or not. Details of the tracking properties of primary and secondary particles of the Monte Carlo code can be found in Ref. [36]. The code calculates, event by event, the total energy released into the six crystals E_γ, which depends on the probability of detecting one or more photon in the same event (summing effect).

In our analysis, which is described in Section 3, the detection efficiency appears in the integral of Eq. (13) together with the effective density profile ρ_{beam}. The absolute detection efficiency at a given z point is:

$$\eta(z) = \frac{N_{det}(z)}{N_{gen}}. \tag{9}$$

Where $N_{det}(z)$ is the number of detected events originating at z point when E_γ is in the ROI (Region of Interest, see Section 3.2), and N_{gen} is the total number of generated events. The typical absolute detection efficiency for the summing peak in the ROI 6.5–8.0 MeV is $65.1 \pm 0.4\%$.

The Monte Carlo predictions have been compared with ^{22}Na and ^{14}N$(p, \gamma)^{15}$O experimental spectra of E_γ. In Fig. 7 is shown the comparison of an experimental ^{22}Na spectrum (solid line, taken at the center of the target chamber, after laboratory background subtraction) with a LUNA Monte Carlo simulation (dotted line). In Fig. 8 the comparison of a high statistics experimental
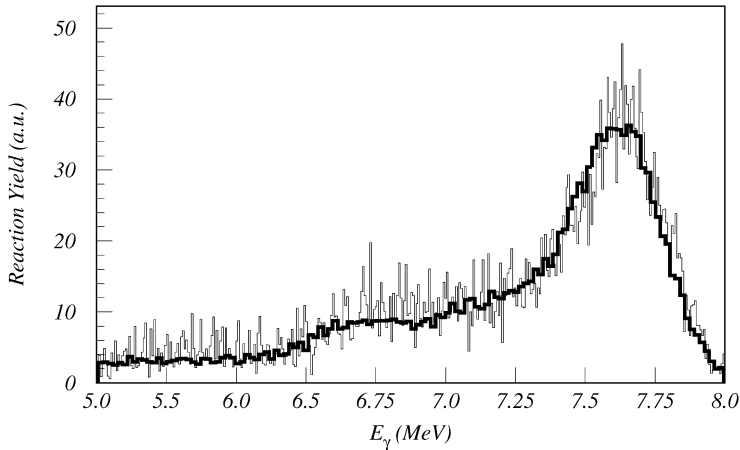
Fig. 8. High statistics background subtracted ^{14}N(p, γ)^{15}O spectrum (thin line, normalized to the beam charge) compared with a simulation (thick line, normalized to ^{14}N(p, γ)^{15}O experimental summing peak) at $E_{\text{beam}} = 237.9$ keV.

spectrum of ^{14}N(p, γ)^{15}O (thin line, after background subtraction, amount of background in the window of the plot is 1.5% of total counts) with a simulation (thick line) is shown.

The code reliability in the description of the complex structure of the γ-ray spectrum (primary and secondary γ-rays, escape peaks, summing effect) is demonstrated by the very good agreement between simulated and experimental data (see Figs. 6, 7 and 8).

2.5. Gamma ray background

The gamma ray background has been studied with a dedicated setup (shown in Fig. 1 of Ref. [38]) and has been already described elsewhere [38]. Briefly, the major sources of background have been identified and localized. The laboratory background counting rate in the ROI is constant and well known (see Section 3.2).

A typical ^{14}N(p, γ)^{15}O spectrum with nitrogen gas is shown in Fig. 9 (solid line). For γ-rays energies below 4 MeV, the spectrum is dominated by the laboratory background (see Figs. 9 and 10). For higher γ-energies, the background induced by the ion beam plays a more prominent role, depending on the beam energies. To evaluate the contribution to the yield from beam induced reactions, monitor runs with helium gas in the target chamber were performed at the same beam energy (to avoid change in beam focusing). This contribution (after laboratory background subtraction) is then rescaled to have equal energy of the proton beam when hitting the beamstop [38] (see Section 3.2).

This procedure has been applied to γ-ray lines that directly appears in the ROI, like the ^{13}C(p, γ)^{14}N reaction ($Q = 7.551$ MeV) that leads to $\simeq 7.7$ MeV γ-rays, superimposed with the sum peak from the reaction to be studied.

Several other reactions lead to γ-rays of $E_{\gamma} > 8$ MeV [38], inducing a small Compton continuum at lower energies. Their contribution to the yield in the ROI was evaluated with the helium monitor runs (after laboratory background and ^{13}C subtraction) and then rescaled to yield of their peaks in the nitrogen spectrum. Single lines from resonant background reactions producing γ-rays in the ROI [38] were fitted and subtracted for runs close to the resonance energy.
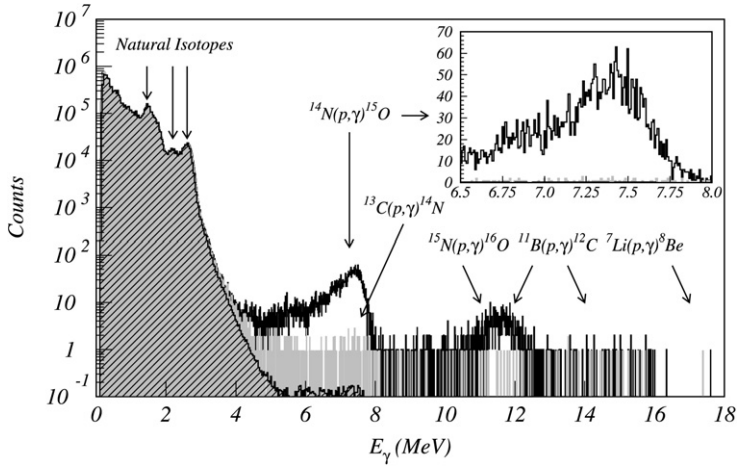
Fig. 9. ^{14}N(p, γ)^{15}O γ-ray spectrum at $E_{\text{beam}} = 141.1$ keV with 1 mbar nitrogen gas (solid line), running time 0.9 day, accumulated charge 19.9 C. ^{14}N(p, γ)^{15}O γ-ray monitor run at same beam energy, normalized to equal lifetime with the nitrogen run, with 1 mbar helium in the target (grey line), running time 1.0 day, accumulated charge 20.8 C. The laboratory background without beam, normalized to equal lifetime with the nitrogen run is also shown (shaded area). In the inset the ^{14}N(p, γ)^{15}O region of interest is expanded.
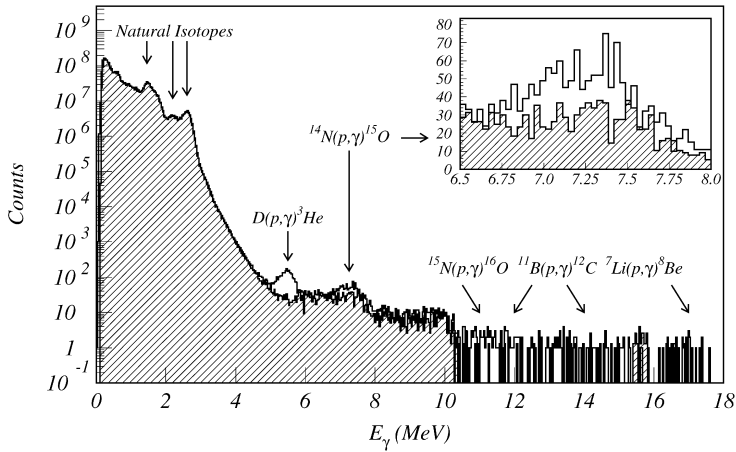
Fig. 10. γ-ray spectrum at $E_{\text{beam}} = 80.9$ keV ($E_{\text{eff}} = 70$ keV, solid line). The running time is 49.12 day and the accumulated charge is 928 ± 8 C. The most relevant beam induced background reactions are indicated. The laboratory background is shaded. In the inset, the region of interest (ROI) for our analysis is enlarged: ^{14}N(p, γ)^{15}O signal (solid line), and laboratory background (shaded area). The beam induced background is discussed in the text.

3. Data analysis

The number of detected counts dN_γ produced in a length dz of the extended nitrogen gas target is given by the expression:

$$dN_\gamma = N_p \sigma(E) \rho_{\text{beam}} \eta \, dz, \tag{10}$$

where N_p is the number of accelerated protons, ρ_{beam} the nitrogen density and η the detection efficiency. The proton beam loses part of its energy passing through the gas target system. The laboratory energy of the projectiles at a given z point is:

$$E(z) = E_{\text{beam}} - \int_0^z \frac{dE}{d(\rho x)}\big(E(z)\big)\rho_{\text{beam}}(z)\,dz, \tag{11}$$

where E_{beam} is the laboratory accelerator beam energy and $\frac{dE}{d(\rho x)}$ is the proton stopping power in the nitrogen gas [34]. Thus, the reaction cross section varies along the beam path. Fusion reaction can therefore take place, with different probability, not only inside the target chamber, but also in the previous stages of the vacuum system and the emitted photons can be detected by the BGO with an efficiency depending on the interaction position (see Fig. 2). Thus the number of detected photons N_γ is given by:

$$N_\gamma = N_p \int_0^L \sigma\big(E(z)\big)\rho_{\text{beam}}(z)\eta(z)\,dz. \tag{12}$$

The length $L = 36.4$ cm is the distance between the first pumping stage, and the calorimeter: this corresponds, according to the Monte Carlo simulation, to the gas target zone where is produced 99.9% of the detected fusion reactions. According to Eq. (1), the ^{14}N(p, γ)^{15}O cross section is expected to be a continuous function at low energies and we can define an effective cross section σ_{eff}, which is the average over the interaction energies:

$$\sigma_{\text{eff}} = \frac{N_\gamma}{N_p \int_0^L \rho_{\text{beam}}(z)\eta(z)\,dz}. \tag{13}$$

From Eq. (13) one obtains the $S(E)$ factor, according to definition (1), provided that an effective interaction energy E_{eff} is introduced.

3.1. Effective interaction energy

We defined the effective energy E_{eff} by the relation:

$$\sigma(E_{\text{eff}}) = \sigma_{\text{eff}}. \tag{14}$$

By inverting Eq. (14) one could obtain $E_{\text{eff}} = \sigma^{-1}(\sigma_{\text{eff}})$. Since $\sigma(E)$ is not known before the measurement, it is not possible to determine E_{eff} directly from experimental data, and a theoretical assumption, eventually coupled with an adaptive iterative method, is needed. In the energy range explored in the experiment, we assumed that the cross section is given by the sum of a non-resonant term plus a Breit–Wigner function for the 259 keV resonance. Since typical values of ΔE_{beam} were about 10 keV in the target, we could assume, for each run below the 259 keV resonance, a constant S factor in Eq. (1) (this introducing an additional uncertainty of 0.1% on the S factor), and thus Eq. (14) reduces to:

$$\frac{e^{-2\pi\eta(E_{\text{eff}})}}{E_{\text{eff}}} = \frac{\int_0^L \frac{e^{-2\pi\eta(E(z))}}{E(z)}\rho_{\text{beam}}(z)\eta(z)\,dz}{\int_0^L \rho_{\text{beam}}(z)\eta(z)\,dz}. \tag{15}$$

The effective interaction energy E_{eff} is simply obtained by inverting the Gamow factor in Eq. (15). With this hypothesis E_{eff} does not depend on the S factor and no iterative correction is needed.

3.2. Experimental uncertainties

The number of detected events, N_γ, is obtained from the BGO spectra after background subtraction:

$$N_\gamma = N_{\text{ROI}} - N_{\text{lab}} - N_{\text{beam}}, \tag{16}$$

where N_{ROI} is the number of photons counted in the 6.5 and 8.0 MeV region of interest (ROI), where the ratio between detection efficiency and background counting rate was maximum [31]; N_{lab} is the number of events due to laboratory background and N_{beam} is the number of counts due to beam induced background, both discussed previously (see Section 2.5). To investigate for possible systematic effects due to the pressure of the monitor run, these measurements were repeated at several helium pressures. We found these effects negligible within 0.2%. In the experiment at high proton energy the background was dominated by the beam induced background and the typical signal to noise ratio ranged from 30 to 60. At low proton energy the background was dominated by the laboratory component. The laboratory background rate in the ROI, without any passive shielding, was 21.1 ± 0.8 counts/day and the lowest counting rate in the present experiment (after background subtraction) was 11.0 ± 0.8 counts/day at $E_{\text{eff}} = 70$ keV.

The statistical uncertainty on N_γ was typically smaller than 3%, and increased up to 7% for the low energy runs. Fig. 10 shows the spectrum collected at $E_{\text{beam}} = 80.9$ keV ($E_{\text{eff}} = 70$ keV), the lowest energy explored in this experiment. It should be noted that, depending on the nominal target pressure, the fraction of detected photons N_γ produced in reactions outside the target cell and in the first aperture (A1 in Fig. 2) varied between 0.5 and 1.5%.

During the experiment the typical beam current was 0.3 mA and the number of accelerated projectiles N_p was obtained by Eq. (2): Its uncertainty depends on those of $W_{\text{no\_beam}}$, W_{beam} and E_{cal}. The quantity $W_{\text{no\_beam}}$ was periodically monitored and we observed a 0.5% fluctuation due to random variation of heat transfer conditions of the calorimeter components. The same fluctuations have been assumed for W_{beam} values. Since $E_{\text{cal}} = E_{\text{beam}} - \Delta E_{\text{cal}}$, where the last term is the total projectile energy loss along the beam path, its uncertainty is affected by those of $\rho_{\text{beam}}(z)$, and by the systematic uncertainty of the hydrogen stopping power in nitrogen gas. For this we adopted the values and recent updates reported in Ref. [34]. The stopping power uncertainty quoted in Ref. [34] is 2.9% (average deviation between fitted curve and experimental data in the energy range between 10 keV and 3 MeV), and the overall agreement for the hydrogen stopping power in all elements is 4.2% [34]. Since we measured at low energies, where the discrepancy between the compilation fitted curve and experimental data looks larger [34], we adopted for the stopping power a conservative uncertainty of 10%. Changing from 2.9% to 10% increases the uncertainty on N_p by less than 0.1%. The typical uncertainty of N_p was 1%, while in the low energy runs increased up to 2%.

The integral in Eq. (13) was calculated by the LUNA Monte Carlo code [36] for the experimental conditions of each run (i.e. beam energy, target pressure, and beam current). The code received as input the measured density profile along the beam path corrected with the beam heating effect (see Section 2.3 and Fig. 5). The uncertainty of the integral in Eq. (13) is affected by those of the density $\rho_{\text{beam}}(z)$, of the detection efficiency $\eta(z)$ and of the Monte Carlo integration which is 0.75%. The uncertainty of the efficiency $\eta(z)$ in the integral of Eq. (13) is affected by those of the decay probabilities to intermediate states of ^{15}O. For it the data reported in Ref. [9] were adopted. We assumed a 10% uncertainty (absolute) of the decay probability values in the entire energy range of our experiment for all the γ-ray transitions. This resulted in a 2.5% systematic uncertainty on the integral in Eq. (13). The recent evidence for an M1 transition to

Table 1
Summary of the experimental uncertainties. See text for details

Quantity	Statistical	Systematic
N_γ	3–7%	
N_p	1–2%	$\leqslant 1\%$
E_{eff}	0.08%	0.56%
$\rho(z)^{\mathrm{a}}$	0.25%	0.5%
$h_{\mathrm{beam}}{}^{\mathrm{a}}$		3.2%
$\eta(z)^{\mathrm{a,b}}$	0.75%	2.9%
$\int_0^L \rho_{\mathrm{beam}}(z)\eta(z)\,dz$	0.79%	4.3%

[a] The uncertainty on this parameter contributes to the overall uncertainty of the integral of Eq. (13) quoted in the last raw of the table.

[b] The statistical uncertainty of the detection efficiency $\eta(z)$ also includes the statistical uncertainty of the Monte Carlo integration technique.

the state at 6.18 MeV [39] does not affect our result within the errors due to the branching ratios quoted above. The angular distribution anisotropy quoted in Ref. [9], thanks to the large solid angle of the BGO detector, affects the efficiency $\eta(z)$ in the integral of Eq. (13) with an uncertainty of 1% only.

In the experiment the target pressure was maintained at 1 mbar, resulting in a beam energy loss of 10 keV. A few runs with target pressure 0.5 and 2.0 mbar were also done to check possible systematic effect. We do not observe any systematic effect on the S-factor, connected to different nitrogen pressure within 1σ level (see Table 2 and Fig. 11).

The beam energy was varied in 10 keV steps between 80 and 250 keV in the laboratory system. The effective energy E_{eff}, defined by Eq. (15) was calculated by the LUNA Monte Carlo code [36]. The numerical integration and inversion of Eq. (15) was better than 10^{-4} (statistical) and 10^{-3} (systematic). The effective energy is also affected by the same uncertainty of E_{cal} quoted above. Since E_{eff} is inside the exponential term, when inverting Eq. (1) its uncertainty affects the astrophysical $S(E)$ factor according to the equation:

$$\left(\frac{\Delta S}{S}\right) = \sqrt{\left(\frac{\Delta\sigma}{\sigma}\right)^2 + \left(1 + \pi\,\eta(E_{\mathrm{eff}})\right)^2 \left(\frac{\Delta E_{\mathrm{eff}}}{E_{\mathrm{eff}}}\right)^2}. \tag{17}$$

Table 1 summarizes the error budget discussed above.

3.3. $\omega\gamma$ factor of the 259 keV resonance

The $\omega\gamma$ strength of the 259 keV resonance was also measured. The method was based on the resonance scan technique, described in Section 2.3, but here using the BGO detector [31]. The beam energy was changed in fine steps (500 eV) to determine the maximum of the reaction yield. The counts collected at the maximum are related to the resonance strength as discussed below.

The 259 keV resonance cross section was described according to the usual Breit–Wigner formula [1]:

$$\sigma(E) = \omega\gamma\,\pi\,\lambda^2(E)\frac{\Gamma_a(E)}{\Gamma_{a\_R}}\frac{\Gamma_b(E)}{\Gamma_{b\_R}}\frac{\Gamma_R}{(E-E_R)^2 + (\Gamma(E)/2)^2}, \tag{18}$$

where λ is the De Broglie wavelength, E_R is the resonance energy, and $\Gamma = \Gamma_a + \Gamma_b$ is the total width of the resonance, Γ_a and Γ_b are the partial width of the decay channel, Γ_{a_R} and Γ_{b_R} are the partial width values at the resonance, $\omega\gamma$ is the strength factor defined as [1]:

$$\omega\gamma = \frac{2J+1}{(2J_1+1)(2J_2+1)}(1+\delta_{12})\frac{\Gamma_{a\_R}\Gamma_{b\_R}}{\Gamma_R}, \tag{19}$$

where J is the resonant state spin and J_1 and J_2 are the spins of the projectile and target nuclei. The energy dependence of the relative partial widths $\Gamma_a(E)/\Gamma_{a\_R}$ and $\Gamma_b(E)/\Gamma_{b\_R}$ have been assumed as in Ref. [1]. For the partial width of the entrance channel $\Gamma_a(E)$ we used the expression [1]:

$$\Gamma_{a,l}(E) = \left(\frac{2E}{\mu}\right)^{1/2}\frac{2\hbar}{R_n}P_l(E,R_n)\theta_l^2. \tag{20}$$

Where μ is the reduced mass (in amu units), R_n is the nuclear radius (in fm units), θ_l^2 is the dimensionless reduced width, l is the orbital angular momentum quantum number, and $P_l(E,R_n)$ is the penetrability. At sub-Coulomb energies ($E \ll E_C$), the penetration factor $P_l(E,R_n)$ is related to the Gamow factor $P_{l=0} = \exp(-2\pi\eta(E))$ by the approximated expression [1]:

$$\frac{P_l(E,R_n)}{P_0(E,R_n)} = e^{-2l(l+1)\left(\frac{\hbar^2}{2\mu Z_1 Z_2 e^2 R_n}\right)^{1/2}} = e^{-7.61\frac{l(l+1)}{(Z_1 Z_2 R_n)^{1/2}}}. \tag{21}$$

Combining the Eqs. (20) and (21) and assuming s wave ($l = 0$), the energy dependence of the relative partial widths $\Gamma_a(E)/\Gamma_{a\_R}$ becomes:

$$\frac{\Gamma_a(E)}{\Gamma_{a\_R}} = \left(\frac{E}{E_R}\right)^{1/2}\frac{e^{-2\pi\eta(E)}}{e^{-2\pi\eta(E_R)}}. \tag{22}$$

Note that for a ΔE of 10 keV the effect of the energy dependence of $\Gamma_b(E)/\Gamma_{b\_R}$ is negligible, while neglecting the energy dependence of $\Gamma_a(E)/\Gamma_{a\_R}$ (Eq. (22)) has an effect of 0.9% on the determination of the $\omega\gamma$ factor. We included both the energy dependence of the relative partial width in our determination of the $\omega\gamma$ strength.

Inserting Eq. (18) in Eq. (12) and solving for the $\omega\gamma$ factor one obtains:

$$\omega\gamma = \frac{N_\gamma}{N_p \int_0^L \pi\lambda^2(E(z))\frac{\Gamma_a(E(z))}{\Gamma_{a\_R}}\frac{\Gamma_b(E(z))}{\Gamma_{b\_R}}\frac{\Gamma_R}{(E(z)-E_R)^2+(\Gamma(E(z))/2)^2}\rho_{\text{beam}}(z)\eta(z)\,dz}. \tag{23}$$

Due to the very high counting rate, the statistical uncertainty of N_γ is negligible. The uncertainty of N_p is about 1%, while the accuracy of $\rho_{\text{beam}}(z)$, and $\eta(z)$ have been discussed above. The integral in Eq. (23) has 2% statistical uncertainty due to the Monte Carlo integration. The stopping power uncertainty quoted above affects the uncertainty of the $\omega\gamma$ strength, through Eq. (11), for 1.6% (included in the values shown in Table 3). The $\omega\gamma$ factor of the 259 keV resonance was measured for three nitrogen pressures (0.5, 1.0, and 2.0 mbar) and the results are discussed in the next section.

4. Results

Table 2 and Fig. 11 summarize the results obtained in the experiment. In Fig. 11, astrophysical S factor values from the present study (filled circles) are compared with previous results: Our data and that from Lamb and Hester [11] (open triangles) have been corrected for electron screening

Table 2

$S(E)$ factor of $^{14}N(p, \gamma)^{15}O$. Data have not been corrected for electron screening effect. The electron screening enhancement factor f [40] applied to the present data for Fig. 11 are also shown

$E_{\text{eff}} \pm \sigma_{E_{\text{eff}}}^{\text{stat}} \pm \sigma_{E_{\text{eff}}}^{\text{syst}}$ (keV)	$\sigma_{\text{eff}} \pm \sigma_{\sigma_{\text{eff}}}^{\text{stat}} \pm \sigma_{\sigma_{\text{eff}}}^{\text{syst}}$ (barn)	$S_{\text{eff}} \pm \sigma_{S_{\text{eff}}}^{\text{stat}} \pm \sigma_{S_{\text{eff}}}^{\text{syst}}$ (keV barn)	f
70.08±0.01±0.09	(2.38±0.19±0.19)×10^{-13}	1.74±0.14±0.14[a]	1.10
79.30±0.02±0.16	(9.82±0.54±0.51)×10^{-13}	1.77±0.10±0.11[a]	1.08
88.70±0.04±0.20	(3.13±0.11±0.10)×10^{-12}	1.70±0.07±0.07[a]	1.07
98.57±0.06±0.40	(9.03±0.49±0.45)×10^{-12}	1.74±0.09±0.10[a]	1.06
108.00±0.09±0.61	(2.06±0.12±0.12)×10^{-11}	1.68±0.10±0.11[a]	1.05
117.59±0.09±0.62	(4.80±0.20±0.23)×10^{-11}	1.81±0.07±0.13[a]	1.05
126.64±0.09±0.64	(9.31±0.39±0.43)×10^{-11}	1.85±0.08±0.13[a]	1.04
136.16±0.09±0.64	(1.84±0.13±0.13)×10^{-10}	1.88±0.08±0.11[a]	1.04
153.26±0.09±0.61	(4.30±0.32±0.19)×10^{-10}	1.86±0.14±0.10[a]	1.03
159.77±0.09±1.02	(6.05±0.22±0.29)×10^{-10}	1.92±0.07±0.13[b,d]	1.03
163.93±0.09±0.61	(7.56±0.36±0.43)×10^{-10}	1.98±0.10±0.13[a,d]	1.03
166.45±0.09±0.41	(9.77±0.45±0.52)×10^{-10}	2.29±0.11±0.13[c,d]	1.03
171.47±0.09±0.54	(1.07±0.04±0.05)×10^{-9}	2.05±0.07±0.10[a]	1.03
181.79±0.09±0.60	(1.88±0.06±0.09)×10^{-9}	2.37±0.08±0.11[a]	1.02
186.61±0.09±0.93	(2.31±0.08±0.11)×10^{-9}	2.44±0.08±0.15[b,e]	1.02
190.34±0.09±0.58	(2.85±0.08±0.12)×10^{-9}	2.63±0.08±0.13[a,e]	1.02
192.60±0.09±0.40	(3.33±0.14±0.18)×10^{-9}	2.85±0.12±0.16[c,e]	1.02
201.01±0.09±0.61	(4.36±0.23±0.19)×10^{-9}	2.81±0.15±0.14[a,f]	1.02
203.48±0.09±0.41	(5.59±0.29±0.24)×10^{-9}	3.33±0.17±0.15[b,f]	1.02
207.82±0.09±0.59	(6.72±0.23±0.30)×10^{-9}	3.49±0.12±0.18[a]	1.02
213.03±0.09±0.98	(8.32±0.28±0.39)×10^{-9}	3.70±0.13±0.21[c,g]	1.02
217.18±0.09±0.58	(1.12±0.04±0.05)×10^{-8}	4.45±0.16±0.23[a,g]	1.02
219.58±0.09±0.39	(1.33±0.05±0.07)×10^{-8}	4.92±0.19±0.25[b,g]	1.02
228.21±0.09±0.58	(2.29±0.07±0.10)×10^{-8}	6.67±0.21±0.32[a]	1.01

[a]Pressure 1.0 mbar; [b]Pressure 2.0 mbar; [c]Pressure 0.5 mbar; [d]Beam energy 181.2 keV; [e]Beam energy 209.1 keV; [f]Beam energy 220.9 keV; [g]Beam energy 237.9 keV.

effect (see Table 2 for details), while this correction was disregarded for all the other data sets. Present data are in agreement, in the overlapping region, with the data of Schröder et al. [15] (open squares). On the contrary, the data of Lamb and Hester [11], obtained with an activation study, are higher than ours. However they report a significant background contribution from the $^{12}C(p, \gamma)^{13}N$ parasitic reaction and an additional 15% systematic uncertainty on detection efficiency and beam intensity [11]. The data of Runkle et al. [28] (capture to the ground state, 6.18 and 6.79 MeV state) have also been included in Fig. 11 for comparison. Finally we find that at low energies our data are significantly lower than the NACRE stellar reaction rate compilation [18] (dashed line).

Table 3 summarizes the values of 259 keV resonance $\omega\gamma$ obtained in the present work and by other authors. The strength value is in very good agreement with Ref. [9]. A reasonable agreement is also found with other works [8,28].

Since there are no experimental data on the electron screening potential U_e for the $^{14}N(p, \gamma)^{15}O$ reaction, we adopted the conservative theoretical values of Assenbaum et al. [40] to compare our data with R-matrix extrapolations (the adopted values of the enhancement factor f are reported in Table 2). At the lowest energies reached in the present work, the electron screening effect from Ref. [40] is comparable with the present experimental uncertainties.
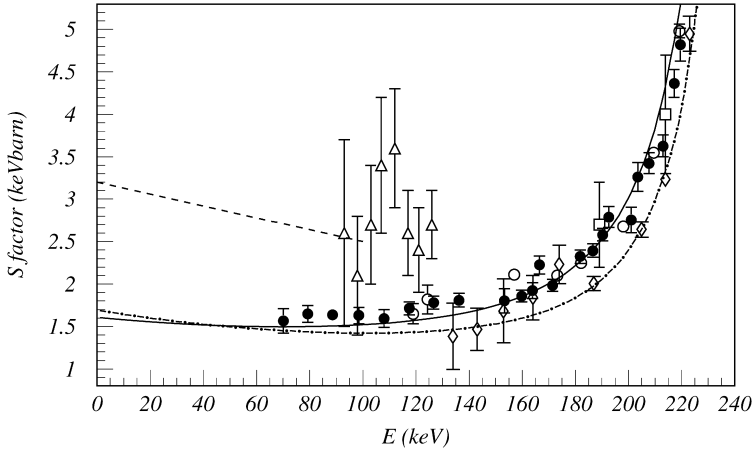
Fig. 11. Astrophysical S factor for the ^{14}N(p, γ)^{15}O reaction from low energy studies: present work (filled circles), Lamb and Hester [11] (open triangles), Schröder et al. [15] (open squares), Imbriani et al. [9] (open circles), Runkle et al. [28] (open diamonds). Recent R-matrix analyses: Imbriani et al. [9] (continuous line), Runkle et al. [28] (dash-dot line), The low energy assumption adopted in the NACRE compilation of stellar reaction rates [18] (dashed line) is also shown. Data and fit from Runkle et al. have been added with R-matrix results from Ref. [9] for the missing transitions.

Table 3
$\omega\gamma$ values of the 259 keV resonance in the ^{14}N(p, γ)^{15}O reaction

Reference	$\omega\gamma$ (meV)
Ajzenberg-Selove [8]	14±1
Runkle et al. [28]	13.5±1.2
Imbriani et al. [9]	12.9±0.4(stat)±0.8(syst)
Present work	12.8±0.3(stat)±0.5(syst)

Recently, the existence of a new resonance in ^{14}N(p, γ)^{15}O at $E_{\text{beam}} = 127$ keV with $\omega\gamma = 4500 \pm 900$ neV was reported [41]. Later on, a dedicated search for this resonance resulted in an upper limit on its $\omega\gamma$ of 32 neV (95% C.L.) [42].

From our data, we deduced a new upper limit of 0.83 neV (2σ level) for the $\omega\gamma$ of this hypothetical resonance. Furthermore, we can quote an upper limit of 0.05 neV (2σ level) on the strength of any resonance in the energy range $E_{\text{beam}} = 80-100$ keV, and of 1.2 neV (2σ level) in the energy range $E_{\text{beam}} = 100-150$ keV.

4.1. ^{14}N(p, γ)^{15}O stellar reaction rate

The Maxwellian averaged reaction rate, $N_A \langle \sigma v \rangle$, (in units of cm^3 mol^{-1} s^{-1}) is computed following the prescription of Ref. [18]:

$$N_A \langle \sigma v \rangle = 3.7313 \times 10^{10} \mu^{-1/2} T_9^{-3/2} \int_0^\infty \sigma(E) E \exp(-11.605 E / T_9) \, dE. \qquad (24)$$
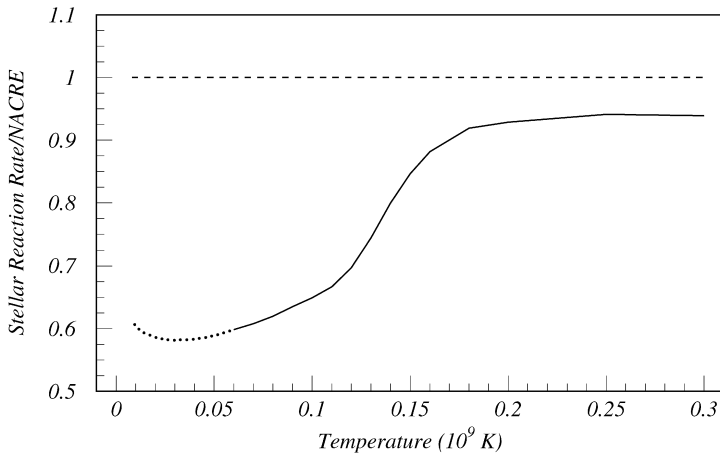
Fig. 12. Stellar reaction rate for the ^{14}N(p, γ)^{15}O reaction relative to the NACRE [18] rate, as a function of the stellar temperature: present work (continuos line, see text for details); NACRE [18] (dashed line); LUNA solid target (Imbriani et al. [9], dotted line).

Where μ is the reduced mass of the system (in units of amu), T_9 is the temperature (in units of 10^9 K), σ is the cross section (in units of barn), and E is the center mass energy (in units of MeV).

The calculation was performed numerically using the present cross section data, corrected for the electron screening effect from Ref. [40] (see Table 2), and the $\omega\gamma$ value of the 259 keV resonance given above. The results are shown in Fig. 12.

For energies $E < 70$ keV, we have assumed a linear relationship for the S-factor based on the R-matrix data from the LUNA solid target experiment (Imbriani et al. [9], Fig. 11).

For temperatures $T_9 > 0.09$, the data from the present work (solid line in the plot) contribute directly for more than 90% to the stellar reaction rate, while the remaining 10% depends on the assumption made for energies $E < 70$ keV.

For temperatures $0.06 < T_9 < 0.09$, the present direct data account for 50–90% of the area under the Gamow peak.

For temperatures $T_9 > 0.18$, the rate from the present work is consistent within the errors with NACRE, but systematically lower by 10%. The reason of this systematic difference is that at these temperatures the stellar reaction rate is dominated by the 259 keV resonance, and our value of the $\omega\gamma$ of this resonance (Section 3.3, Table 3) is lower than the value of $\omega\gamma = 14 \pm 1$ meV adopted in the NACRE compilation [18].

For $T_9 < 0.18$, non-resonant capture becomes more and more important, and at these temperatures the present rate is up to 40% lower than NACRE since the S factor values are much lower than the NACRE extrapolation (Fig. 11).

4.2. Astrophysical consequences

The data obtained in the present experiment has been used to directly evaluate the reaction rate for several important stellar scenarios, with negligible impact from the extrapolation applied at lower energies.

Low mass stars burn first hydrogen and then helium in their center. After the end of the helium burning phase, the star consists of a degenerate core of oxygen and carbon and two shells burning

hydrogen and helium, respectively. This phase of stellar evolution is called the Asymptotic Giant Branch (AGB) [43]. It is characterized by flashes of the helium burning shell that spawn convective mixing in a process called dredge-up. Such a dredge-up transports the products of nuclear burning from inner regions of the star to its surface, where they are in principle accessible to astronomical observations.

The temperature in the hydrogen burning shell of an AGB star is of the order of $T_9 = 0.05$–0.08 for the example of a $2M_\odot$ star ($M_\odot$: mass of our Sun) with metallicity $Z = 0.01$. It has been shown [44] that an arbitrary 25% reduction of the $^{14}\text{N}(p, \gamma)^{15}\text{O}$ rate with respect to the NACRE [18] rate leads to twice as efficient dredge-up of carbon to the surface of the star, because the rate of energy generation in the hydrogen burning shell becomes even lower than before, enhancing the disequilibrium between hydrogen and helium burning shell. The CNO rate suggested by the present study is more than 25% below the NACRE [18] rate. Still, the change in the $^{14}\text{N}(p, \gamma)^{15}\text{O}$ rate might lift a disagreement between model and observation for so-called carbon stars [45]: For low (i.e. $2M_\odot$) mass stars, models do not reproduce a sufficiently high carbon content in the atmosphere.

Recently, a simulation for a $5M_\odot$, $Z = 0.02$ AGB star [46] found stronger thermal flashes for a reduced CNO rate, consistent with the finding of Ref. [44] for a $2M_\odot$, $Z = 0.01$ AGB star.

For a zero metallicity (population III) star of $1M_\odot$, after a sufficient amount of carbon has been created in the triple-α reaction, the CNO cycle is ignited in the so-called CN flash. This CN flash takes place at $T_9 \approx 0.065$ and leads to a brief loop of the trajectory of the star in the Hertzsprung–Russell diagram [47]. With a CNO rate that is 40% lower than the NACRE [18] rate, this loop disappears [46]. Also, the first core helium flash in such a star was found to be less luminous than in the reference case, albeit with a higher core mass, as a result of a lower CNO rate [46].

Temperatures of $T_9 \approx 0.1$ correspond to CNO burning in heavy ($20M_\odot$) population III stars [48]. Explosive burning in novae [49] takes place at even higher temperatures, typically $T_9 \approx 0.2$. The $^{15}\text{N}/^{14}\text{N}$ isotopic ratio in nova ashes depends sensitively on the $^{14}\text{N}(p, \gamma)^{15}\text{O}$ rate [50]; the more precise rate that can be calculated from the cross sections obtained in the present study will reduce the uncertainty of the isotopic ratio.

5. Conclusion

The total cross section of the $^{14}\text{N}(p, \gamma)^{15}\text{O}$ reaction, the bottleneck of the CNO cycle, has been measured down to $E = 70$keV, well within the energy window where stellar CNO hydrogen burning takes place. The strength of the $E_R = 259$ keV resonance has been determined with improved precision, and stringent upper limits have been put on possible narrow resonances between $E_{\text{beam}} = 80$–150 keV. The reaction rate for several scenarios of hydrogen burning, both stable and explosive, has been calculated directly from the present cross section data, with negligible impact from the assumptions made for the cross section at lower energies. The impact of the present rate on nucleosynthesis in AGB stars of different masses ($M = 1$–$20M_\odot$), in particular the carbon content of the atmosphere and the luminosity of the core helium flash, and on explosive burning in novae ($^{15}\text{N}/^{14}\text{N}$ isotopic ratio) has been discussed.

Acknowledgements

References

[1] C. Rolfs, W.S. Rodney, Cauldrons in the Cosmos, University of Chicago Press, 1988.
[2] S.P. Ahlen, et al., Phys. Lett. B 249 (1990) 149.
[3] P. Belli, et al., Nuovo Cimento A 101 (1989) 959.
[4] U. Greife, et al., Nucl. Instrum. Methods Phys. Res. A 350 (1994) 327.
[5] A. Formicola, et al., Nucl. Instrum. Methods Phys. Res. A 507 (2003) 609.
[6] R. Bonetti, et al., Phys. Rev. Lett. 82 (1999) 5205.
[7] C. Casella, et al., Nucl. Phys. A 706 (2002) 203.
[8] F. Ajzenberg-Selove, Nucl. Phys. A 523 (1991) 1.
[9] G. Imbriani, et al., Eur. Phys. J. A 25 (2005) 455.
[10] D.B. Duncan, J.E. Perry, Phys. Rev. 82 (1951) 1304.
[11] W. Lamb, R. Hester, Phys. Rev. 108 (1957) 1304.
[12] R.E. Pixley, The reaction cross section of nitrogen 14 for protons between 220 keV and 600 keV, PhD Thesis, California Institute of Technology, August 1957.
[13] B. Povh, D.F. Hebbard, Phys. Rev. 115 (1959) 608.
[14] D.F. Hebbard, G.M. Bailey, Nucl. Phys. 49 (1963) 606.
[15] U. Schröder, et al., Nucl. Phys. A 467 (1987) 240.
[16] G. Caughlan, W. Fowler, At. Data Nucl. Data Tables 40 (1988) 283.
[17] E. Adelberger, et al., Rev. Mod. Phys. 70 (1998) 1265.
[18] C. Angulo, et al., Nucl. Phys. A 656 (1999) 3.
[19] C. Angulo, P. Descouvemont, Nucl. Phys. A 690 (2001) 755.
[20] P.F. Bertone, et al., Phys. Rev. Lett. 87 (2001) 152501.
[21] P.F. Bertone, et al., Phys. Rev. C 66 (2002) 055804.
[22] A. Mukhamedzhanov, et al., Phys. Rev. C 67 (2003) 065804.
[23] K. Yamada, et al., Phys. Lett. B 579 (2004) 265.
[24] A. Formicola, et al., Phys. Lett. B 591 (2004) 61.
[25] J.N. Bahcall, M.H. Pinsonneault, Phys. Rev. Lett. 92 (2004) 121301.
[26] S. Degl'Innocenti, et al., Phys. Lett. B 590 (2004) 13.
[27] G. Imbriani, et al., Astron. Astrophys. 420 (2004) 625.
[28] R.C. Runkle, et al., Phys. Rev. Lett. 94 (2005) 082503.
[29] A. Lemut, et al., Phys. Lett. B 634 (2006) 483.
[30] D. Bemmerer, Experimental study of the ^{14}N(p, γ)^{15}O reaction at energies far below the Coulomb barrier, PhD Thesis, Technische Universität Berlin, August 2004.
[31] A. Lemut, Misura della sezione d'urto della reazione ^{14}N(p, γ)^{15}O ad energie di interesse astrofisico, PhD. Thesis, Università degli Studi di Genova, April 2005.
[32] C. Casella, et al., Nucl. Instrum. Methods Phys. Res. A 489 (2002) 160.
[33] S.K. Allison, Rev. Mod. Phys. 30 (1958) 1137.
[34] H.H. Andersen, J.F. Ziegler, Stopping Powers and Ranges in All Elements, Pergamon, 1977 (updated data are available online at http://www.srim.org).
[35] J. Görres, et al., Nucl. Instrum. Methods 177 (1980) 295.
[36] C. Arpesella, et al., Nucl. Instrum. Methods Phys. Res. A 360 (1995) 607.
[37] H. Costantini, et al., Phys. Lett. B 482 (2000) 43.
[38] D. Bemmerer, et al., Eur. Phys. J. A 24 (2005) 313.
[39] S.O. Nelson, et al., Phys. Rev. C 68 (2003) 065804.
[40] H. Assenbaum, et al., Z. Phys. A 327 (1987) 461.
[41] S.O. Nelson, et al., Bull. Am. Phys. Soc. 46 (2001) 64.
[42] R.C. Runkle, et al., Phys. Rev. C 66 (2002) 022801.
[43] I. Iben, A. Renzini, Annu. Rev. Astron. Astrophys. 21 (1983) 271.
[44] F. Herwig, S.M. Austin, Astrophys. J. 612 (2004) L73.
[45] I. Iben, Astrophys. J. 246 (1981) 278.
[46] A. Weiss, et al., Astron. Astrophys. 441 (2005) 1129.

[47] A. Weiss, et al., Astrophys. J. 533 (2000) 413.
[48] L. Siess, M. Livio, J. Lattanzio, Astrophys. J. 570 (2002) 329.
[49] J. Jose, M. Hernanz, Astrophys. J. 494 (1998) 680.
[50] C. Iliadis, et al., Astrophys. J. Suppl. Ser. 142 (2002) 105.